



UNIVERSITÀ DI PARMA

ARCHIVIO DELLA RICERCA

University of Parma Research Repository

Long fatigue crack growth in Inconel 718 produced by selective laser melting

This is the peer reviewed version of the following article:

Original

Long fatigue crack growth in Inconel 718 produced by selective laser melting / Konečná, R; Kunz, L.; Nicoletto, Gianni; Bača, A.. - In: INTERNATIONAL JOURNAL OF FATIGUE. - ISSN 0142-1123. - 92:(2016), pp. 499-506. [10.1016/j.ijfatigue.2016.03.012]

Availability:

This version is available at: 11381/2816106 since: 2021-10-13T14:59:25Z

Publisher:

Elsevier Ltd

Published

DOI:10.1016/j.ijfatigue.2016.03.012

Terms of use:

Anyone can freely access the full text of works made available as "Open Access". Works made available

Publisher copyright

note finali coverpage

(Article begins on next page)

LONG FATIGUE CRACK GROWTH IN INCONEL 718 PRODUCED BY SELECTIVE LASER MELTING

R. Konečná^a, L. Kunz^b G. Nicoletto^c, A. Bača^a,

^a*University of Žilina, Department of Materials Engineering, Univerzitná 1, 01026 Žilina,
Slovakia*

^b*Institute of Physics of Materials, Academy of Sciences of the Czech Republic,
Žižkova 22, 61662 Brno,
Czech Republic*

^c*University of Parma, Department of Industrial Engineering, Parco Area delle Scienze,
181/A, 43100 Parma,
Italy*

ABSTRACT

Growth of long fatigue cracks **is** investigated in Inconel 718 superalloy produced by selective laser melting (**SLM**). The fatigue crack growth curve and the threshold value of the stress intensity factor **are** experimentally determined on compact-tension specimens fabricated using a RENISHAW A250 system and the recommended processing parameters.

The crack propagation curve and the crack propagation threshold of this SLM material **are** compared with literature data describing the behavior of conventionally manufactured Inconel 718. The fatigue crack growth **is** discussed in terms of the specific microstructure and residual stresses produced by selective laser melting.

KEYWORDS

Inconel 718; selective laser melting; microstructure; fatigue crack growth; fractography.

Introduction

Conventionally manufactured Inconel 718 is high-strength corrosion resistant nickel chromium superalloy frequently used for **high-temperature** applications (up to 700 °C) like jet engines and high-speed airframe parts, gas turbines, exhaust manifolds or turbochargers. The microstructure of this solution annealed and precipitation hardened alloy consists of a nickel-rich γ matrix, which has a face-centered cubic (fcc) lattice structure with many different precipitates. The fine grain size is sought because it leads to high yield and ultimate tensile strength as well as good fatigue strength. Outstanding high-temperature mechanical properties of Inconel 718 are induced by particle strengthening effect of secondary precipitates and solid solution hardening. The major part of the strengthening at elevated temperatures is caused by the secondary precipitates γ' and γ'' [1-5]. Though this alloy can be readily fabricated even into complex parts and its welding characteristics are favorable, the industry is interested in production of parts utilizing the advantages of rapidly developing additive layer manufacturing technologies. Selective laser melting (SLM) has recently gained a lot of interest due to the feasibility of producing metallic components directly from a computer-aided design file of the part. The technology has strong impact on variety of industries, e.g. aerospace, medical or automotive [6].

SLM is a very complex process with a number of non-equilibrium phenomena depending on the process details. The microstructure of the final product fabricated by localized melting and solidification of gas atomized Inconel 718 powder is strongly influenced by process parameters like the laser power and the beam diameter, scanning parameters and, indeed, the starting material powder. The microstructure substantially differs from that produced by the conventional manufacturing process. Moreover, the thermal conductivity, temperature and **environmental** conditions in the process chamber of the SLM system play an important role.

The static performance of many SLM materials was found to be reasonably comparable in terms of the ultimate strength, yield strength and elongation to conventionally manufactured materials. **Because** of the advantages of the SLM technology, there is a strong tendency to apply it even where not only the static but also fatigue properties are required for reliable and **long-term** operation of components. Due to the complex interaction of SLM process parameters, resulting microstructure and material properties, the needed fatigue design data reflect the particular parameters set in the process, because the fatigue behavior appears highly susceptible to phenomena **such** as porosity, build orientation, residual stress

and surface conditions [7-9]. Because the SLM fabrication route is increasingly applied to Inconel 718, its fatigue behavior and the fatigue crack propagation data are desirable for a more widespread use.

This study is aimed at the determination of long fatigue crack growth data and on the characterization of microstructure of Inconel 718 manufactured by SLM. The long crack growth and the mechanism of crack tip interaction with the specific SLM microstructure during crack propagation are discussed.

Material, specimens and experiments

The powder of pre-alloyed atomized Inconel 718 **has been** used to prepare the compact-tension (CT) specimens. The granulometry of powder **is** in the range from 20 to 50 μm . Scanning electron microscope image of the shape and size powder particles are shown in Fig. 1. The chemical composition of **the** final product determined by glow discharge spectrometry in wt. % is the following: 51.6 Ni, 18.8 Cr, 18.6 Fe, 5.36 Nb, 3.14 Mo, 0.378 Co, 0.970 Ti, 0.498 Al, 0.156 Cu, 0.0932 W, 0.0781 V, 0.101 Mn, 0.0198 Zr, 0.0732 C, 0.00976 P, 0.00318 B, 0.00529 S and 0.0938 Si.

The CT specimens for fatigue crack growth testing **have been** produced by SLM on a RENISHAW A250 machine. This system features a vacuum chamber which, after low-pressure atmospheric evacuation, allows the refill of the chamber with high purity argon gas. A soft blade evens out each fresh layer of powder material across the surface of the bed before consolidation by the laser. The machine is equipped with a fiber laser (wavelength $\lambda = 1070$ nm) with a maximum power of 200 W. All specimens **have been** made at the full laser power. The modulated pulsed-laser moves in a raster fashion 50 μm point-to-point and with a point exposure time of 251 μs . The scanning speed **is** approximately 200 mm/s. The lateral separation between consecutive scan lines **has been** set at 180 μm whereas the layer thickness **has been** fixed at 50 μm . The selective layer-by-layer melting of the powder by the laser beam induces an inherent texture in the SLM material. Consequently, the parts have some degree of anisotropy.

The CT specimens with characteristic **size** $w = 30$ mm and thickness $t = 6$ mm according to the geometry specified in ASTM E 647-08 **have been** fabricated by the SLM process. The crack propagation direction **has been** identical with the build direction, see Fig. 2. The as-produced CT specimen is shown in Fig. 3. It is pointed out that the pin holes and the starter notch **have been** obtained directly. The pin holes **have then been** reamed to the

final tolerance.

Specimens for metallographic analysis **have been** cut out from as-produced CT specimen after fatigue testing in such a way that the microstructure in the three main planes defined in Fig. 2 could be visualized. Specimens **have been** hot-pressed into Duroplast using CitoPress-1 device. Surfaces for observation **have been** prepared using an automatic grinding and polishing system TegraPol-15. Grinding was conducted using SiC paper (220 grit) and fine sanding on the **MD** Largo discs with the addition of DiaProAlegro Largo emulsion. Polishing **has been** conducted using MD Dac canvas with the addition of DiaProDac emulsion, followed by a final chemical polishing on the MD Chem polishing wheel with the addition of OP-S suspension.

The metallographic analysis **has been** performed using light microscope (LM) Neophot 32 and Zeiss Axio Observer Z1M on specimens etched by Kalling's reagent (2 g of CuCl_2 , 40 ml of HCl, 80 ml of methanol). After re-polishing and etching by agent with composition 40 ml HNO_3 + 30 ml HF specimens used for LM have further been investigated by scanning electron microscopy (SEM) using Tescan LYRA 3 XMU FEG/SEM system.

Vickers hardness determination **has been** performed using 250 HPO/AQ apparatus. The load of 98.1 N (10 kp) **has been** applied for 10 s.

The fatigue crack growth (FCG) experiments **have been** conducted on a Roell/Amsler HFP 5100 resonant testing machine in load control under load cycle asymmetry $R = P_{\min}/P_{\max} = 0.1$. The loading frequency **is** dependent on the crack length, i.e. on the stiffness of the cracked specimen and **is** in the interval from 80 to 60 Hz. Crack propagation measurement **is** performed G at ambient laboratory conditions. The crack length **is** optically measured checking the two lateral sides of the specimen, which **have been** ground and mechanically polished. The resolution of the determination of the crack tip position by means of CCD cameras with suitable optics **is** 0.01 mm. The measurement **fulfils** the requirements of the ASTM E647-08 standard.

The fatigue growth tests **have been** started at load amplitudes resulting in initiation of a fatigue crack from the starting chevron notch after some hundreds of thousand cycles. When the crack **has** appeared on both lateral sides of the specimen, the load amplitude shedding procedure fulfilling the load ratio condition $R = 0.1$ **has been** applied to reach the crack growth rate of about 1×10^{-6} mm/cycle. Then the load amplitude **has been** held constant, and the real determination of the crack growth rate **has been** started after the crack **growth** through the area influenced by the load shedding procedure.

The lowest crack growth rates of the order of 1×10^{-7} mm/cycle in the threshold region

have been reached by load shedding method. The load is reduced in steps which are of 10 % of the preceding value at most. As valid data are considered only those which are determined after the crack grows through the corresponding cyclic plastic zone and when the average crack increment on both sides of the specimen is larger than 0.1 - 0.2 mm.

Fatigue fracture surfaces are investigated by means of SEM with the aim to describe the peculiarities of the crack propagation in the microstructure produced by SLM.

Results

Microstructure

As-fabricated CT specimens produced by SLM exhibit strong directionality of the microstructure, Fig. 4. The micrographs taken at lower magnifications by optical microscopy reveal the SLM process characteristics: line-by-line and then layer-by-layer building-up of the bulk. In x-z and y-z planes (vertical sections) the microstructural characteristics are similar, Fig. 4 a, b. The cut of the melted tracks shows series of arcs produced by the laser energy distribution. The circular melt pools, and layered structure appears as the result of the laser beam alternating motion in x-y plane perpendicular (cross section) to the build direction, Fig. 4c. The maximum diameter, indicated by the arrows (Fig. 4a, b), reaches up to 100 μm . The average layer thickness is of about 40 μm .

Each next layer overlaps the previous melt pool tracks, and due to heating influences the microstructure of the previous layer. All melted tracks are closely stacked to form a good metallurgical bonding between two neighboring layers. Defects in the form of small microshrinkages between the connected layers have been found only rarely in the microstructure. Similarly, small gas pores manifesting themselves as black round spots have been observed only locally. The observed layer structure and melt pool tracks are typical features of the SLM production in various materials [10, 11] when the build strategy is of the type used in this study.

The microstructure at a higher magnification, Fig. 5a, is characterized by columnar grains (oriented in the build direction) with two different types of microstructure, indicated as 1 and 2. The microstructure corresponding to region 1 is characterized by very small cuboidal particles of γ'' -bct (body centered tetragonal structure) Ni_3Nb precipitates (Fig. 5b) in solid solution γ (Ni-Cr) fcc matrix. Columnar grains appear as elongated columns in the form of very fine dendrites in the region 2, Fig. 5c. This structure is a result of grain growth at very high cooling rates. Long columnar grains preferably develop in the direction parallel to the

build direction.

Fine γ'' cuboidal particles are typical microstructural units within the melt pools, Fig. 6a. The size of γ'' particles inside the melt pool areas is much smaller than that in the columnar grains outside the melting pools. Their size is often smaller than 1 μm . The elongated structure, Fig. 6b, at very high magnification appears as ellipsoidal particles.

The Vickers hardness of the SLM produced material does not depend within (the scatter of measurement) on the plane orientation with respect to the build direction. The hardness measured on the x-y plane is $\text{HV}_{10} = 330 \pm 11$, whereas that on the z-y plane is $\text{HV}_{10} = 338 \pm 11$. The average value of Vickers hardness corresponds to the Rockwell hardness 34 HRC, which is a typical value for precipitation hardened Inconel 718 manufactured by conventional techniques [12].

Fatigue crack growth

The experimentally determined points of the crack growth curve describing the behavior of long cracks in the investigated SLM Inconel 718 are shown in Fig. 7. The crack growth rate da/dN is plotted against the stress intensity factor range $\Delta K = (K_{\text{max}} - K_{\text{min}})$. It can be seen that a linear dependence fits well the experimental points for crack growth rates higher than 1×10^{-6} mm/cycle. Below this rate, the crack growth curve tends to reach the threshold and the typical knee appears. All experimental points, $[da/dN; \Delta K]$, for rates higher than 1×10^{-6} mm/cycle can be well approximated by the following equation:

$$da/dN = 4.54 \times 10^{-8} \Delta K^{2.3}, \quad (1)$$

which is represented by the dashed line. From the data in Fig. 7, the lowest value of the stress intensity factor range ΔK at which the crack growth rate is reliably measurable is $3.0 \text{ MPam}^{1/2}$ for $R = 0.1$. This value can be considered the threshold value ΔK_{th} of the present SLM material. Taking into account this, all experimental points including the threshold region can be well described by the following equation:

$$da/dN = 5 \times 10^{-8} (\Delta K^{2.3} - \Delta K_{\text{th}}^{2.3}), \quad (2)$$

which is represented by the full line.

Fractography

The local crack growth rate is determined by the applied stress intensity factor, local microstructure and residual stresses. Examples of characteristic fracture surfaces, as observed by SEM, are presented in Figs. 8 and 9.

The fatigue fracture surface corresponding to the crack growth rate of 8×10^{-7} mm/cycle and the stress intensity factor range $\Delta K = 4.0 \text{ MPam}^{1/2}$ (i.e. near the threshold) is shown in Fig. 8 (note that the macroscopic crack propagation direction is from top to bottom). The macroscopic plane of the fracture surface is parallel to the building direction of SLM process. The crack propagates in a transgranular manner. The fracture surface is characterized by many parallel secondary cracks, which are often markedly opened. The secondary cracks are indicated in Fig. 8a by arrows. The average distance of the parallel secondary cracks is of about $0.5 \mu\text{m}$, which is a value nearly three orders of magnitude larger than the average crack increment at the corresponding crack growth rate.

The variability of the fracture surface in the near threshold region is demonstrated in Fig. 8b, where the secondary cracks are rarely observed. The fracture surface is again transgranular without any specific fractographic features, see region A. Region B is characteristic by elongated areas covered by fine slip lines. No secondary cracks are visible here. Arrows in Fig. 8 indicate the local direction of the crack growth. It locally differs a lot from the macroscopic crack propagation direction.

The fracture surface corresponding to the crack propagation in the Paris region is shown in Fig. 9. The surface has been created by the crack propagating at growth rate of 1×10^{-5} mm/cycle. The appearance is very similar to that shown in Fig. 8. In comparison to the threshold region, some of the secondary cracks are longer and more open. The traces of slip lines are also visible, see arrow in Fig. 9b.

Well-developed striations appear at high crack growth rates reaching 1×10^{-4} mm/cycle. An example is shown in Fig. 10. The striation distance roughly corresponds to the macroscopic crack growth rate.

Fatigue fracture profiles

The fracture profiles as observed by LM on polished and etched sections in y-z plane direction and perpendicular to the fracture surface are shown in Fig. 11. The crack growth direction is from right to left (arrow in Fig. 11a). The fatigue crack propagates in the threshold region in a transgranular way, and is obviously not influenced by the specific SLM microstructure. The fracture profile view corresponding to $\Delta K = 3.2 \text{ MPam}^{1/2}$ and $da/dN \sim 10^{-7}$ mm/cycle is flat with local small sharp asperities (Fig. 11a). Secondary cracks emanating from the main crack do not have any visible relation to the microstructure. Fig. 11b shows the crack profile typical for the Paris region. The only difference is in the roughness of the

fracture profile, which is **more significant** when compared to the roughness of the fracture profile in Fig. 11a. The crack propagation remains transgranular.

Discussion

Inconel 718 produced by SLM in contrast to the conventionally manufactured alloy exhibits strong features of local directional solidification. The SLM CT specimens exhibit a columnar microstructure [13] which **is also confirmed** in this investigation (Figs. 4 and 5). Microstructure of parallel elongated fine columns (Fig. 5a, c) was characterized in [14, 15] as a fine columnar microdendritic structure. The sections of fine columns by a metallographic plane inclined at a high angle to their long axis have an ellipsoidal shape (Fig. 5c, Fig. 6b) with dimensions obviously dependent on the mutual orientation of columns and the metallographic section. The cuboidal structure corresponds to the γ'' precipitates. The preferred formation of γ' rather than γ'' precipitations has been shown to be dependent on Ti + Al/Nb ratio [2, 3]. Cozar et al. [3] concluded that, if the Ti + Al/Nb ratio is above a critical value (from 0.9 to 1), the γ' precipitates formation prevails over the γ'' formation. In some cases, special cube-shaped γ' particles coated with a γ'' shell **can be** identified. This effect is related to very slow coarsening rate [3]. Amato et al. [13] confirmed (with XRD spectra) the presence of γ matrix and γ'' precipitates in the structure of Inconel 718.

The propagation of long cracks in conventionally manufactured Inconel 718 at ambient and high temperatures was studied quite intensively in the past, e.g. [16-21], because this alloy is often used for fabrication of components exposed to long term cyclic loading at high temperatures. Also the mechanism of the crack growth was a subject of investigation. The threshold values for propagation of long cracks have been shown to be dependent on temperature and microstructure. Yamada et al. [20] **have recently** presented a detailed study on the effect of crack closure on the crack growth in Inconel 718 in the wrought state. Their measurements indicate a threshold value in the range $\Delta K_{th} = 8 - 10 \text{ MPam}^{1/2}$ at $R = 0.1$, which is attributed to the anticipated crack closure phenomenon affecting the loading cycle. On the other hand, the near-threshold FCG data at $R = 0.8$ and higher, which are expected to be crack closure free, define a ΔK_{th} **value** of about $3 \text{ MPam}^{1/2}$.

The fatigue crack growth curves, particularly in the threshold region, were shown to be dependent on the chemical composition. The content of boron ranging from 12 to 100 ppm decreases the crack growth rate substantially [22]. The loading with the stress intensity factor

range $\Delta K = 10.0 \text{ MPam}^{1/2}$ in the case of the lowest B concentration results in a crack growth rate of $1 \times 10^{-6} \text{ mm/cycle}$ as in the material with the highest B content loaded at $\Delta K = 14.4 \text{ MPam}^{1/2}$ [22].

Contrary to the case of conventionally manufactured alloy, the knowledge on the mechanical properties of SLM Inconel 718 is limited. As regards the tensile properties, they are comparable to those of the wrought material [23]. Influence of processing parameters, like atmosphere in the building chamber, was reported, but these effects seem to be weak. On the other hand, the comparison of the fatigue crack growth curves of wrought and SLM manufactured alloy shows substantial differences.

Fig. 12 brings the comparison of the crack propagation curves of SLM and conventionally manufactured alloys at the same load ratio $R = 0.1$. The data by Clavel and Pineau [17] were determined on similar CT specimens. The crack growth rates above $5 \times 10^{-5} \text{ mm/cycle}$ in both materials can be considered as identical within the data scatter band. A strong difference, however, appears in the near-threshold region. The resistance of the present SLM Inconel 718 against crack growth is substantially lower. Similar conclusions can be drawn when data for SLM material are compared with results, by Yuen et al. [18]. The crack growth data by Mercer et al. [19] coincide with those by Clavel and Pineau in the threshold region, but the crack growth rate is slightly lower in the Paris region. The data by Osinkolu et al. [21] correspond well to the data by Clavel and Pineau, though this measurement was performed for slightly lower value of R , namely $R = 0.05$. Threshold values (for $R = 0.1$) in the range $\Delta K_{th} = 8\text{-}12 \text{ MPam}^{1/2}$ were also determined by Yamada and Newman [20]; these values are substantially higher than the present SLM threshold data.

Generally, it can be concluded that SLM and conventionally manufactured Inconel 718 have nearly identical resistance to the growth of long cracks for loading in the high ΔK region. Very severe difference, however, can be found in the threshold region. The threshold stress intensity factor range ΔK_{th} of SLM material based on the crack growth rate $1 \times 10^{-7} \text{ mm/cycle}$ is only 25 % of the value determined in [17, 19] and 40 % of the value found by Yuen et al. [18].

The explanation of the very low threshold value of SLM alloy tested in this work can be substantiated by (i) low B content, (ii) the specific microstructure, (iii) by the presence of residual stresses.

Low values of the threshold found in this work are consistent with the observation made on the conventionally manufactured Inconel. Decreasing the B content (from 100 to 12 ppm)

significantly increases the crack growth rate and decreases the threshold [22]. The boron content in our material is low, namely 0.00318 wt %, which corresponds to 32 ppm. This fact is consistent with the observed low threshold.

The investigated alloy exhibits very fine grain. The grain size is of about 10 μm , whereas the alloy studied by Clavel and Pineau [16] had grain size equal to 30 μm . This finding is consistent with the general trend of decreasing threshold with decreasing grain size. The fracture profile presented in Fig. 11a shows that the fatigue crack propagates in the threshold region through the microstructure without any specific interference with the structural features, like grain boundaries. No correspondence of the fatigue crack paths and the melt pool tracks or particular building layers can be identified. The crack propagation is of transgranular manner, which is well documented in Figs. 8 and 9. The fracture surface is very similar to that reported for conventionally manufactured alloy [16, 19].

The SLM produced components are characterized by high residual stresses, see for example [24] in the case of Ti-6Al-4V. Strong differences in the crack propagation rate in the as-built and after stress relief were found and were attributed to the modified residual stress systems. In the present case, the SLM IN718 specimens are in the as-produced state. Considering that the crack growth direction is parallel to the build direction, Fig. 2, and that the material around the starter notch is selectively melted last, a system of tensile residual stresses is expected to affect the notch root and favor closure-free crack growth. If that were the case, the present SLM IN718 alloy near threshold FCG data could be compared to the surely crack closure free data (at $R = 0.8$) of wrought Inconel 718, [20]: such a comparison shows a coincident value of ΔK_{th} equal to about 3 $\text{MPam}^{1/2}$. Therefore, residual stresses may have a key role in the interpretation of the FCG behavior of SLM materials. Research activity on this topic are needed.

The mechanism of the crack propagation is based on the planar cyclic slip in the region ahead the main crack tip. The cyclic slip is localized on parallel slip planes. The cycling leads to a gradual damage of suitably oriented slip bands and formation of microcracks. Some of them are significantly opened. The main crack propagates by their linking or by rupture of areas in which the slip activity due to inconvenient orientation is weak. This mechanism is similar to that known from conventionally manufactured alloy [23]. The mechanism of the crack growth in the near-threshold region and in the Paris region is basically the same. The only difference is in the extent of the cyclically loaded volume, which increases with increasing ΔK and the size of the cyclic plastic zone. Higher cyclic slip activity and larger

plastic zone at higher ΔK is reflected on the fracture surface by more opened and larger microcracks. The crack path is entirely transgranular for crack rates ranging from the threshold region up to the end of the Paris region.

At crack growth rates reaching 1×10^{-4} mm/cycle, formation of striations is observed, Fig. 10. This witnesses for the change of mechanism of fatigue crack growth to ductile at high ΔK values. The plastic blunting model of crack growth can be considered as appropriate for crack advance description at high crack growth rates. Similar behavior was reported for conventionally manufactured alloy [23]. Simultaneously, the da/dN vs. ΔK curves of both alloys are identical in this crack growth region.

Conclusions

1. The propagation of long cracks at room temperature and at stress ratio $R = 0.1$ in Inconel 718 manufactured by selective laser melting can be well described by equation $da/dN = 4.54 \times 10^{-8} \Delta K^{2.3}$ in the Paris region, or by equation $da/dN = 6.0 \times 10^{-8} (\Delta K^{2.3} - \Delta K_{th}^{2.3})$ in the threshold and Paris region. The threshold value of the stress intensity factor is $\Delta K_{th} = 3.0 \text{ MPa m}^{1/2}$. For the loading with the stress intensity factor range exceeding $20 \text{ MPa m}^{1/2}$, the crack growth resistance of SLM and wrought alloys is nearly identical.
2. The behavior of the present SLM Inconel 718, which is apparently less resistant to the growth of long cracks in the near-threshold region than the conventionally manufactured alloy, has been discussed in terms of the expected influence of residual stresses, low content of boron and finer microstructure.
3. Fatigue crack growth occurs in transgranular mode. The cyclic plasticity is localized into parallel slip bands. The mechanism of the crack growth at threshold and in the Paris region consists in the formation of microcracks ahead of the main crack. The main crack grows by their linking. At high crack growth rates, the mechanism of crack growth changes, and the occurrence of striations is observed. On the microscopic level, the local direction of crack growth is dependent on the grain orientation.
4. The microstructure of SLM Inconel 718 exhibits specific features related to the building process. The melt pools are typical by fine grained microstructure and very small precipitates. The remaining volume is composed of coarse columnar grains having often elongated microstructure. The defects in the form of small voids and cavities are rare.

Acknowledgements

The authors wish to acknowledge the company Protoservice srl., Forno Taro, Italy for providing the Inconel 718 specimens produced by SLM. The research is supported by project VEGA grant No. 1/0685/2015 and is realized in the frame of the Strategy AV21 Academy of Sciences of the Czech Republic.

References

- [1] Zhang, H. Y., Zhang, S. H., Cheng, M., Li, Z. X., *Materials Characterization* 61 (2010) 49–53.
- [2] Kirman, I., Warrington, O. H., Precipitation in nickel-based alloys containing both niobium and titanium. *J. Inst. Metals* 99 (1971) 197–202.
- [3] Cozar, R., Pineau, A., Morphology of γ' and γ'' precipitates and thermal stability of Inconel 718 type alloys. *Metall. Trans.* 4 (1973) 47–59.
- [4] Sundararaman, M., Mukhopadhyay, P., Banerjee, S., Some aspects of the precipitation of metastable intermetallic phases in Inconel 718. *Metall. Trans.* 23A (1992) 2015–2028.
- [5] Durand-Charre, M., Davidson, J. H., *The microstructure of superalloys*, Gordon and Breach Science Publ., Amsterdam (1997) 124.
- [6] Kruth, J. P., Levy, G., Klocke, F., Childs, T. H. C., Consolidation phenomena in laser and powder-bed based layered manufacturing, *CIRP Ann. Manuf. Technol.*, 56 (2007) 730–759.
- [7] Gu, D., Shen, Y., Balling phenomena in direct laser sintering of stainless steel powder: Metallurgical mechanisms and control methods, *Materials and Design* 30 (2009) 2903–2910.
- [8] Janaki Ram, G. D., Venugopal Reddy, A., Prasad Rao, K., Reddy, G. M., Sarin Sundar, J. K., Microstructure and tensile properties of Inconel 718 pulsed Nd-YAG laser welds. *Journal of Materials Processing Technology* 167 (2005) 73–82.
- [9] Murr, L. E., et al., Microstructural architecture, microstructures, and mechanical properties for a nickel-base superalloy fabricated by electron beam melting, *Metall. Trans. A* 42A (2011) 3491–3508.
- [10] Jinhui, L., Ruidi, L., Wenxian, Z., Linding F., Huashan, Y. *Material Science and Technology* 26 (2010) 1259-1264.

- [11] Yadroitsev, I., Thivillion, L., Bertrand, Ph., Smurnov, I. Applied Surface Science 254 (2007) 980-983.
- [12] Kruth, J. P., Badrossamay, M., Yasa, E., Deckers, J., Thijs, L., Van Humbeeck, J., Part and material properties in selective laser melting of metals. 16th International Symposium on Electromachining (ISEM), (2010), Shanghai, China.
- [13] Amato K. N., et al., Microstructures and mechanical behavior of Inconel 718 fabricated by selective laser melting, Acta Mater. 60 (2012) 2229–2239.
- [14] Jia, Q., Gu, D., Selective laser melting additive manufacturing of Inconel 718 superalloy parts: Densification, microstructure and properties, J. Alloys Comp. 585 (2014) 713–721.
- [15] Wang, Z., Guan, K., Gao, M., Li, X., Chen, X., Zeng, X., The microstructure and mechanical properties of deposited-IN718 by selective laser melting, J. Alloys Comp. 513 (2012) 518–523.
- [16] Clavel, M., Pineau, A., Frequency and wave-form effects on the fatigue crack growth behavior of alloy 718 at 298 and 823 K, Metall. Trans A 9A (1978) 471-480.
- [17] Clavel, M., Pineau, A., Fatigue behavior of two nickel-base alloys. I. Experimental results on low cycle fatigue, fatigue crack propagation and substructures. Mat. Sci. Eng. A 55 (1982) 157-171.
- [18] Yuen, L. J., Roy, P., Nix, W. D., Effect of oxidation kinetics on the near threshold fatigue crack growth behavior of a nickel base superalloy, Metall. Trans A 15A (1984) 1769-1775.
- [19] Mercer, C., Soboyejo, A. B. O., Soboyejo, W. O., Micromechanisms of fatigue crack growth in a forged Inconel 718 nickel-based superalloy. Mat. Sci. Eng. A270 (1999) 308-322.
- [20] Yamada, Y., Newman Jr., J. C., Crack closure under high load-ratio conditions for Inconel-718 near threshold behavior, Eng. Fract. Mech., 76 (2009) 209-220.
- [21] Osinkolu, G. A., Onofrio, G., Marchionni, M, Fatigue crack growth in polycrystalline IN 718 superalloy. Mat. Sci. Eng. A356 (2003) 425-433.
- [22] Xiao, L., et al., Effect of boron on fatigue crack growth behavior in superalloy IN 718 at RT and 650 °C, Mat. Sci. Eng. A 428 (2006) 1-11.
- [23] Andersson, H., Persson, C., In-situ SEM study of fatigue crack growth behaviour in IN718, Int. J. Fatigue 26 (2004) 211–219.
- [24] Vrancken, B., Cain V., Knutsen, R., Van Humbeeck, J., Residual stress via the contour method in compact tension specimens produced via selective laser melting,

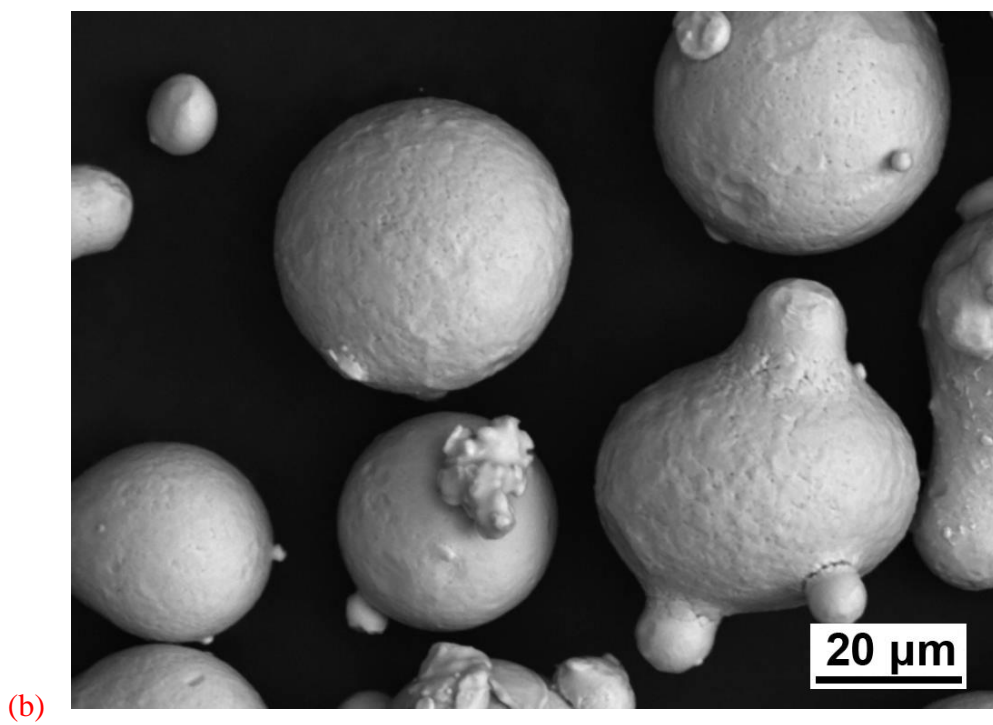
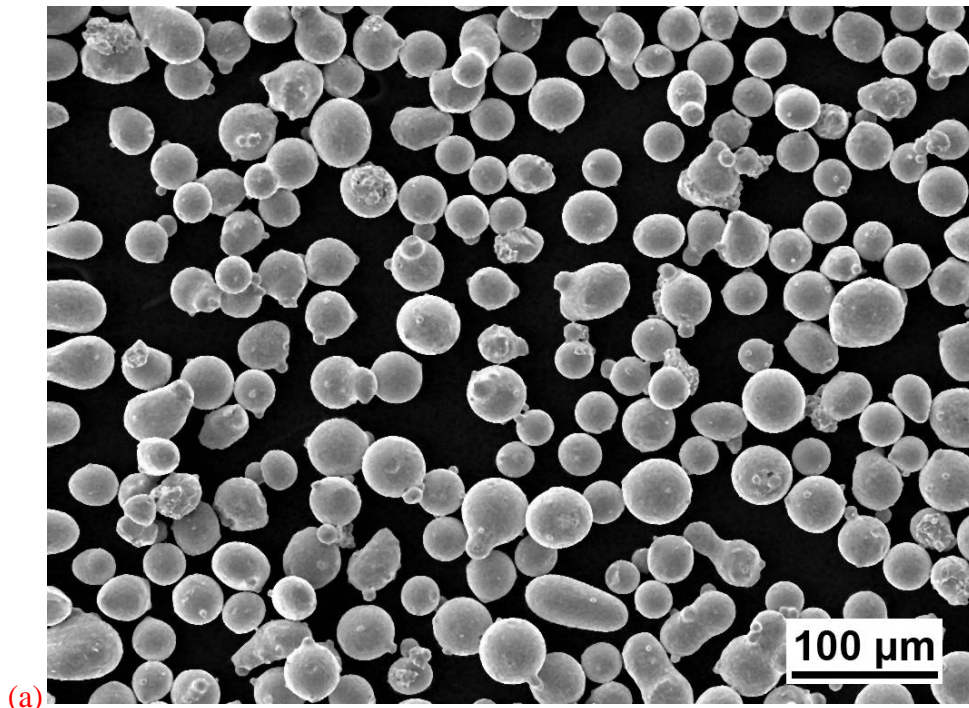


Fig. 1 Powder of IN 718; (a) shape of powder, (b) detail of granules shape, SEM

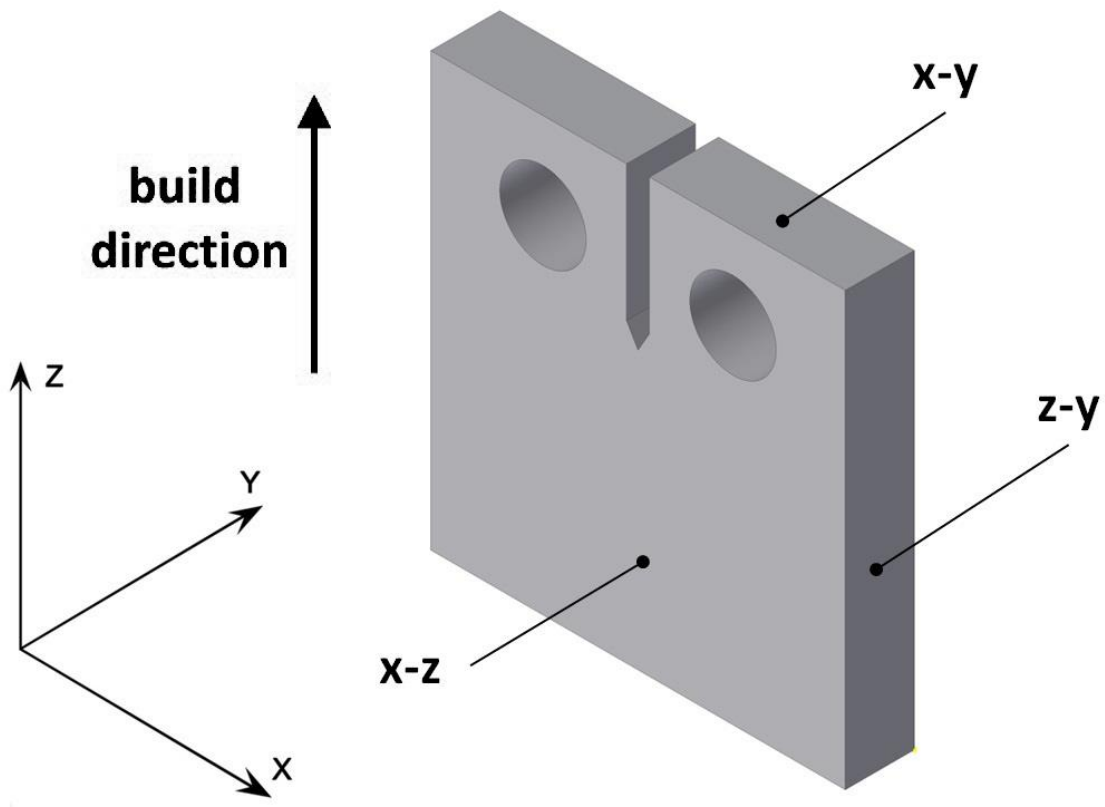


Fig. 2 Orientation of CT specimen and main planes with respect to the build direction

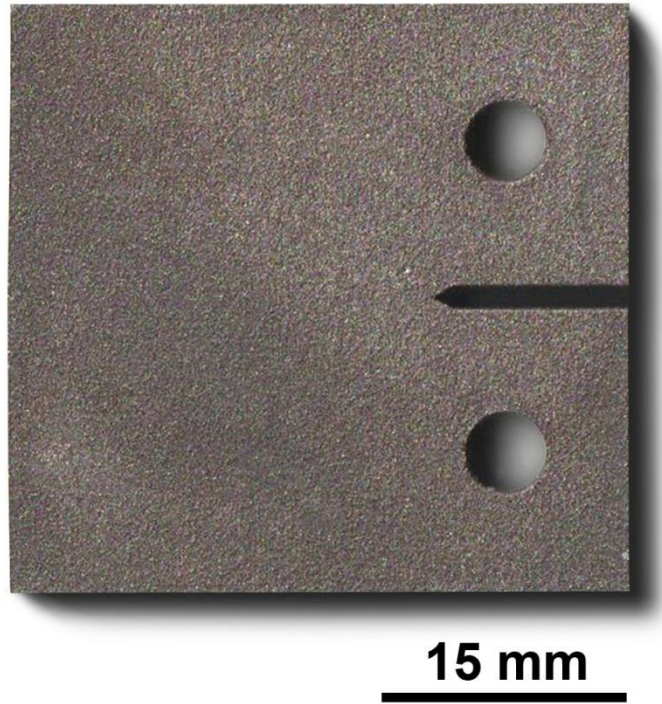
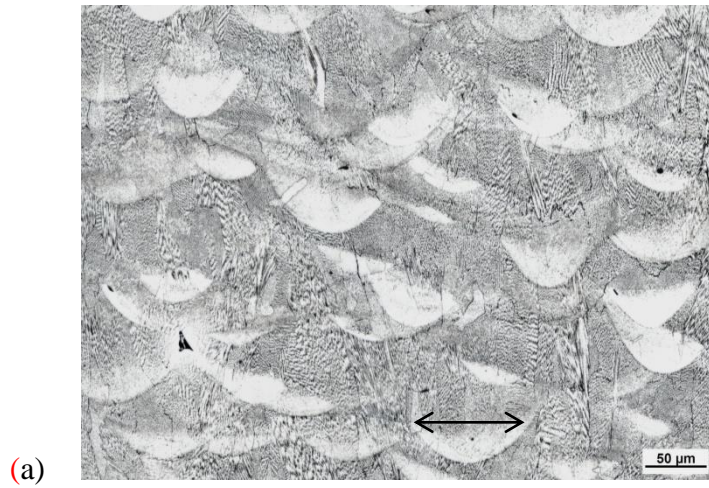


Fig. 3 CT specimen as produced by SLM process



+



Fig. 4 Characteristic texture of Inconel 718 on (a) x-z plane, (b) y-z plane, (c) x-y plane, LM

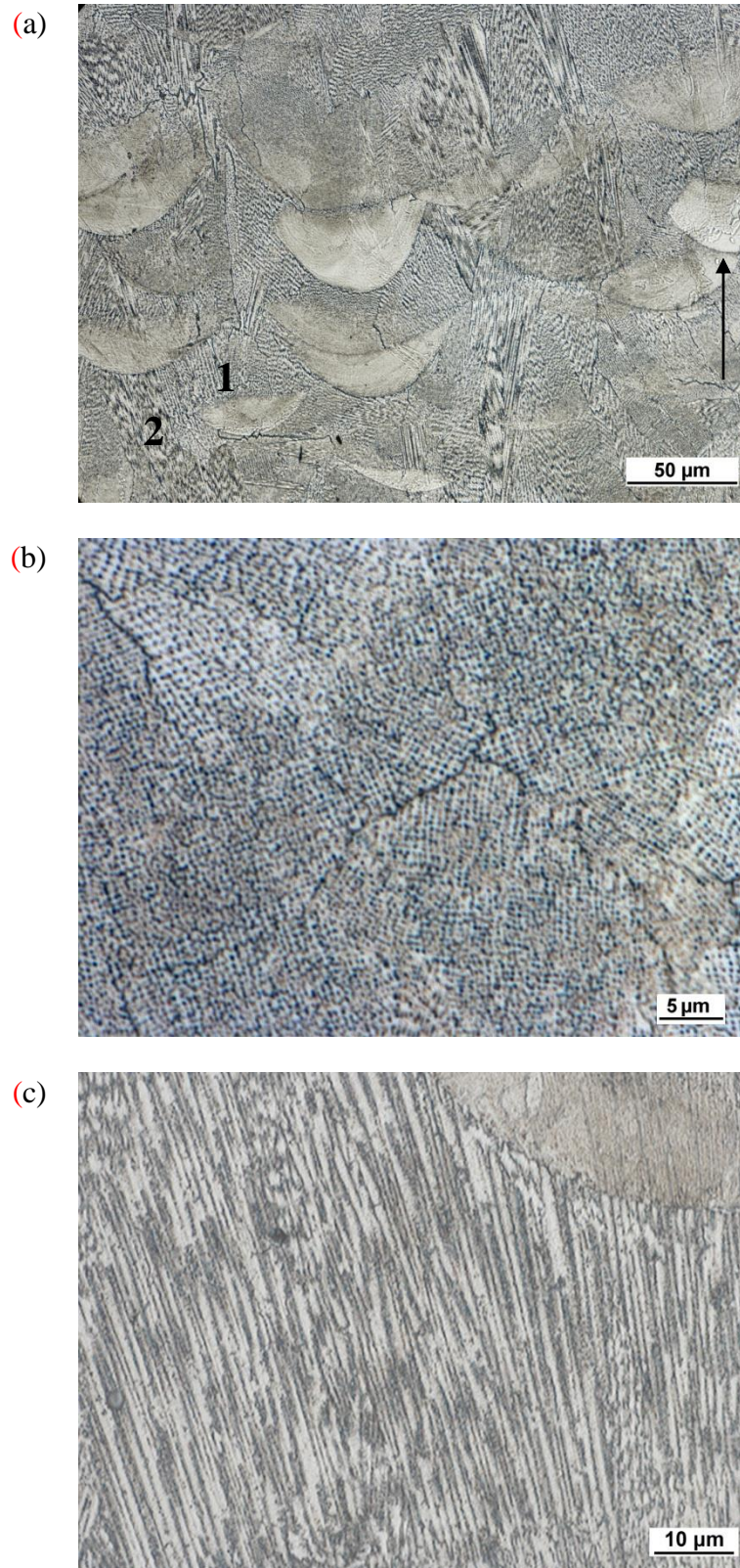


Fig. 5 Microstructure of IN 718 produced by SLM on x - z plane: (a) melt bends and irregular columnar arrays with two different structures (arrow indicates the build direction); (b) 1-cuboidal particles (precipitates); c) 2-elongated microdendritic structure, LM

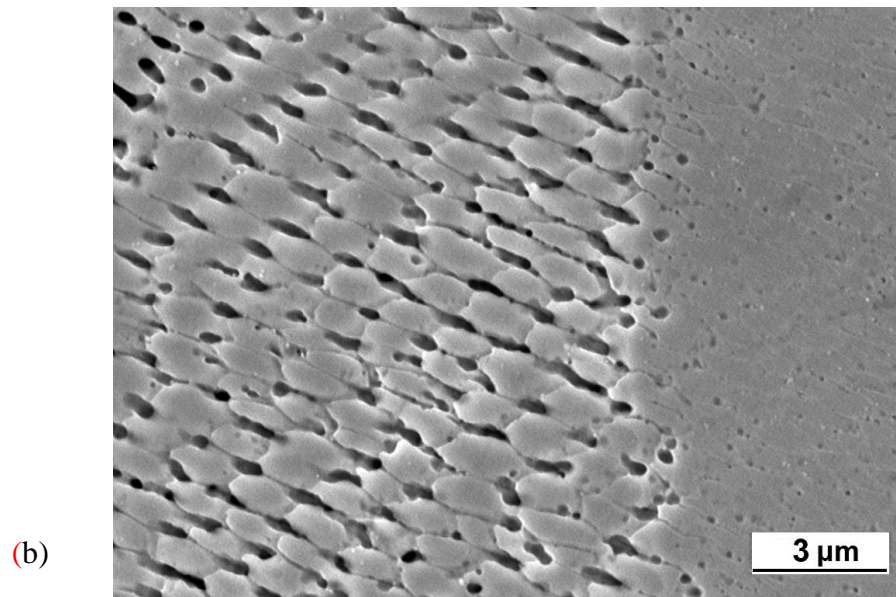
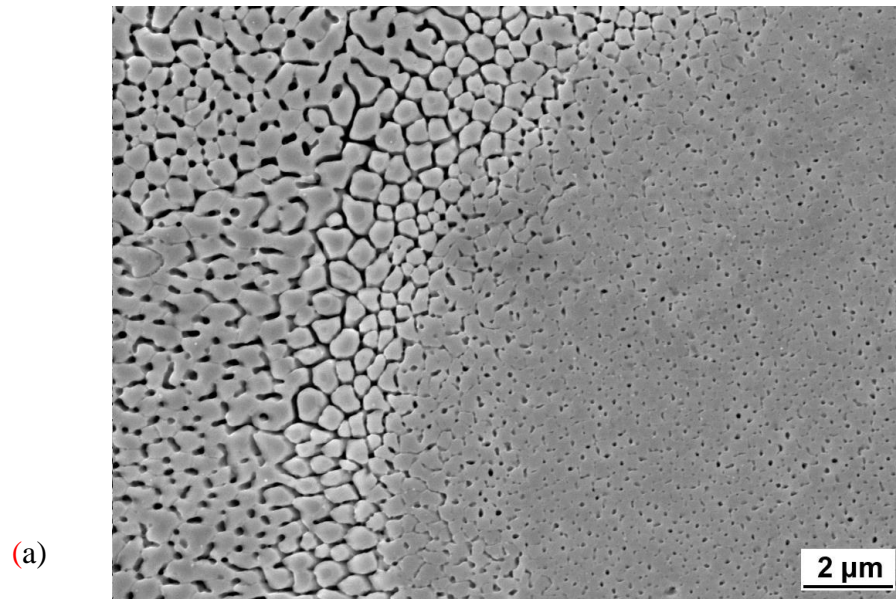


Fig. 6 Detail of microstructure in the in the x-y plane: (a) cuboidal particles, (b) ellipsoidal particles, SEM

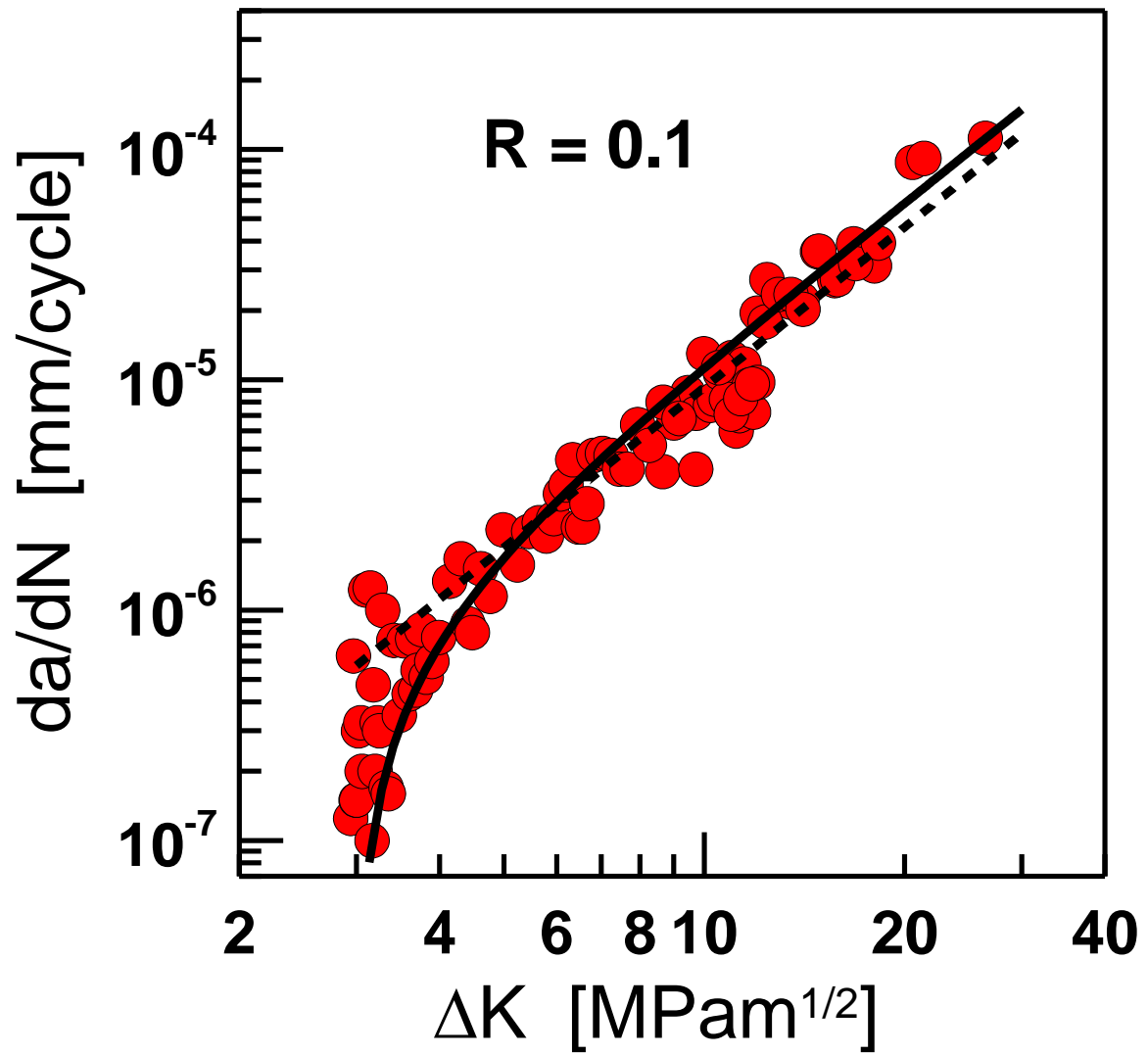


Fig. 7 Fatigue crack growth data for IN 718 alloy manufactured by SLM

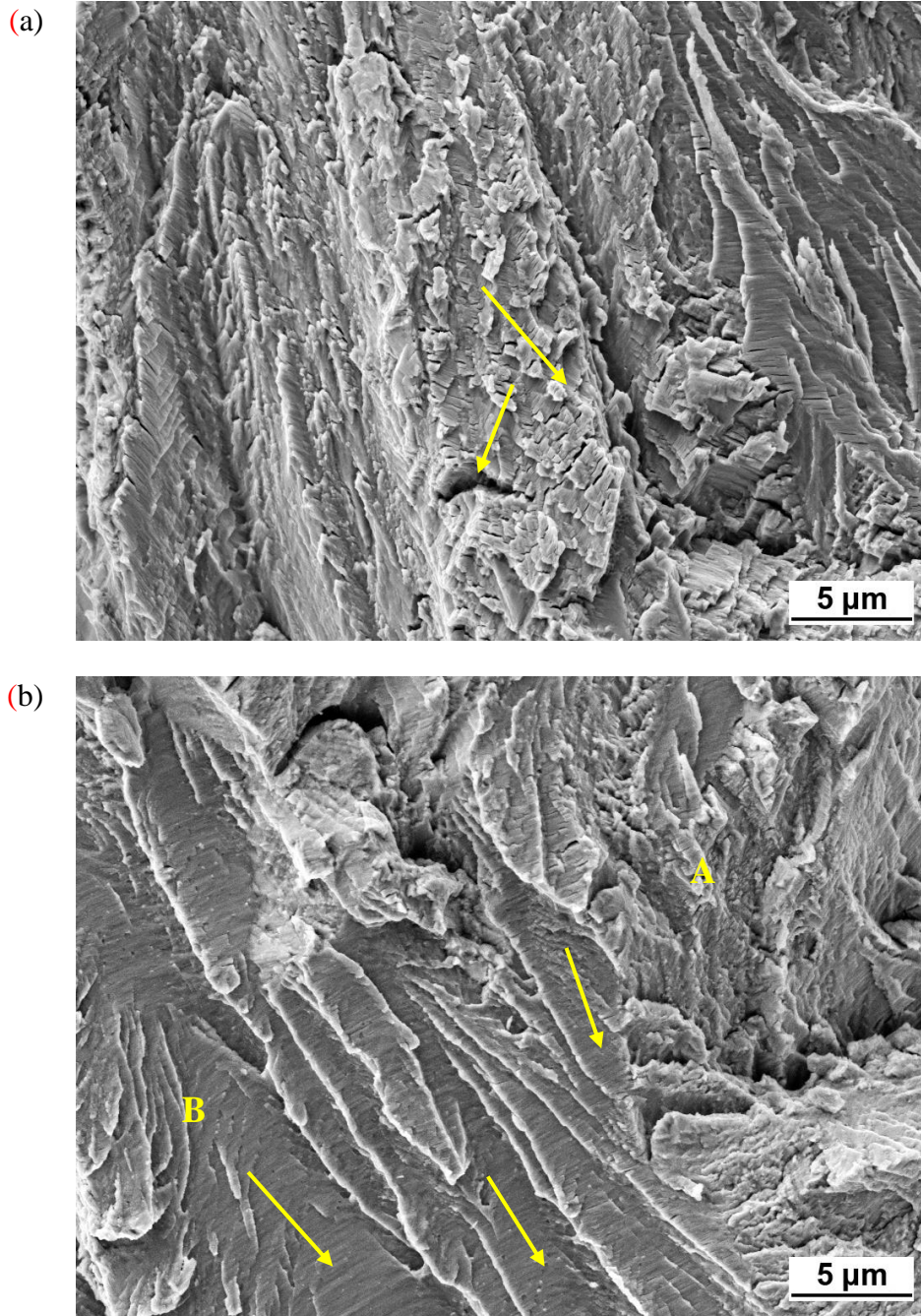


Fig. 8 Fracture surface corresponding to the average crack rate 8×10^{-7} mm/cycle

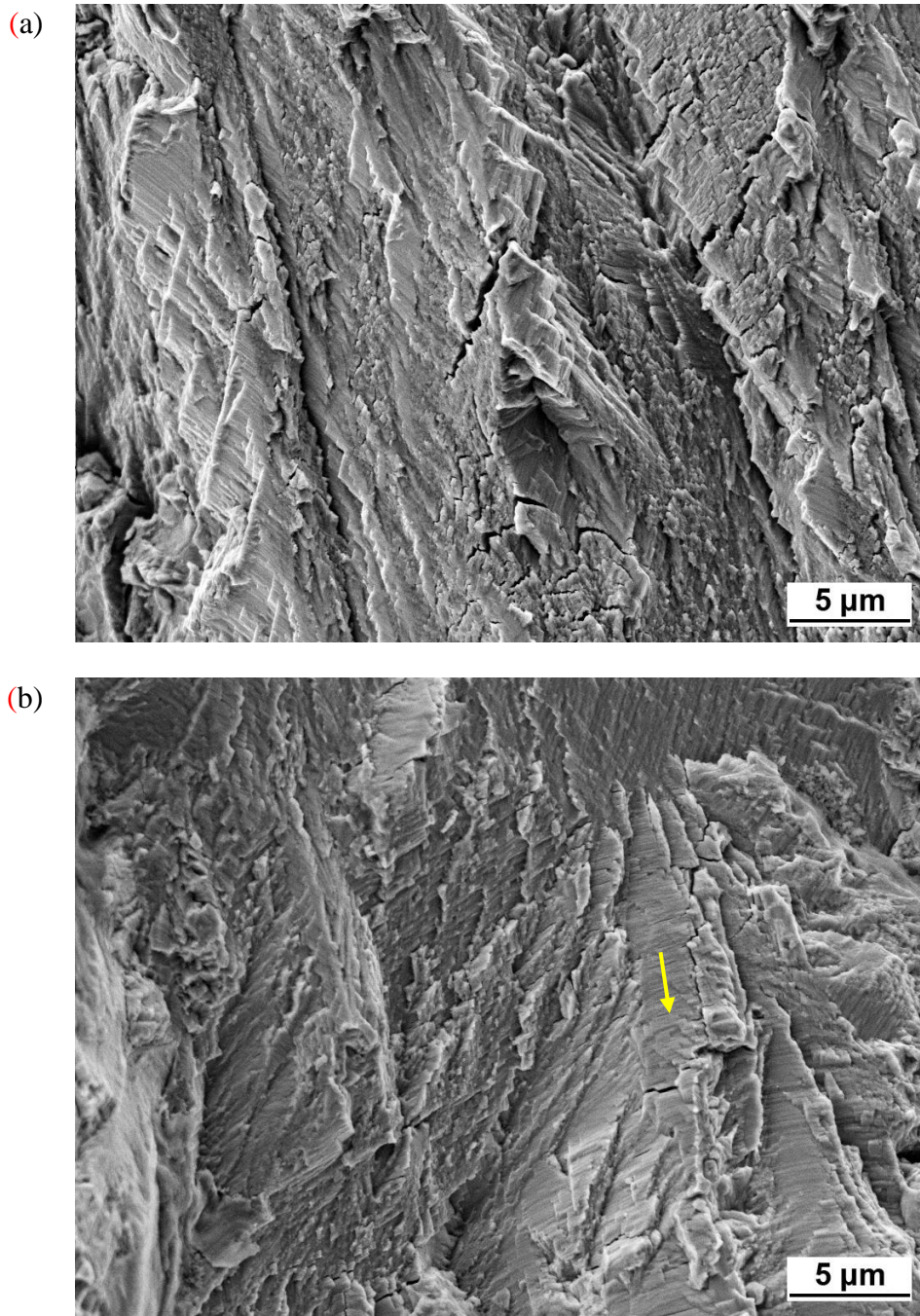


Fig. 9 Fracture surface corresponding to the average crack rate 1×10^{-5} mm/cycle

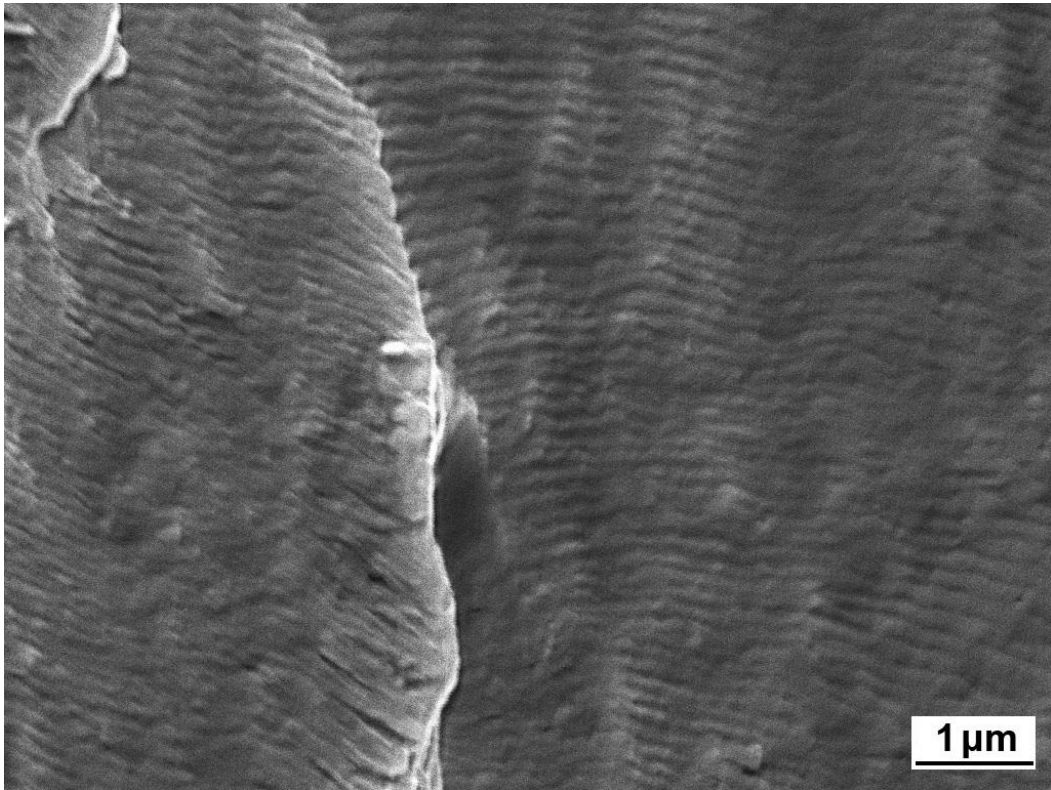


Fig. 10 Fracture surface corresponding to the crack growth rate 1×10^{-4} mm/cycle

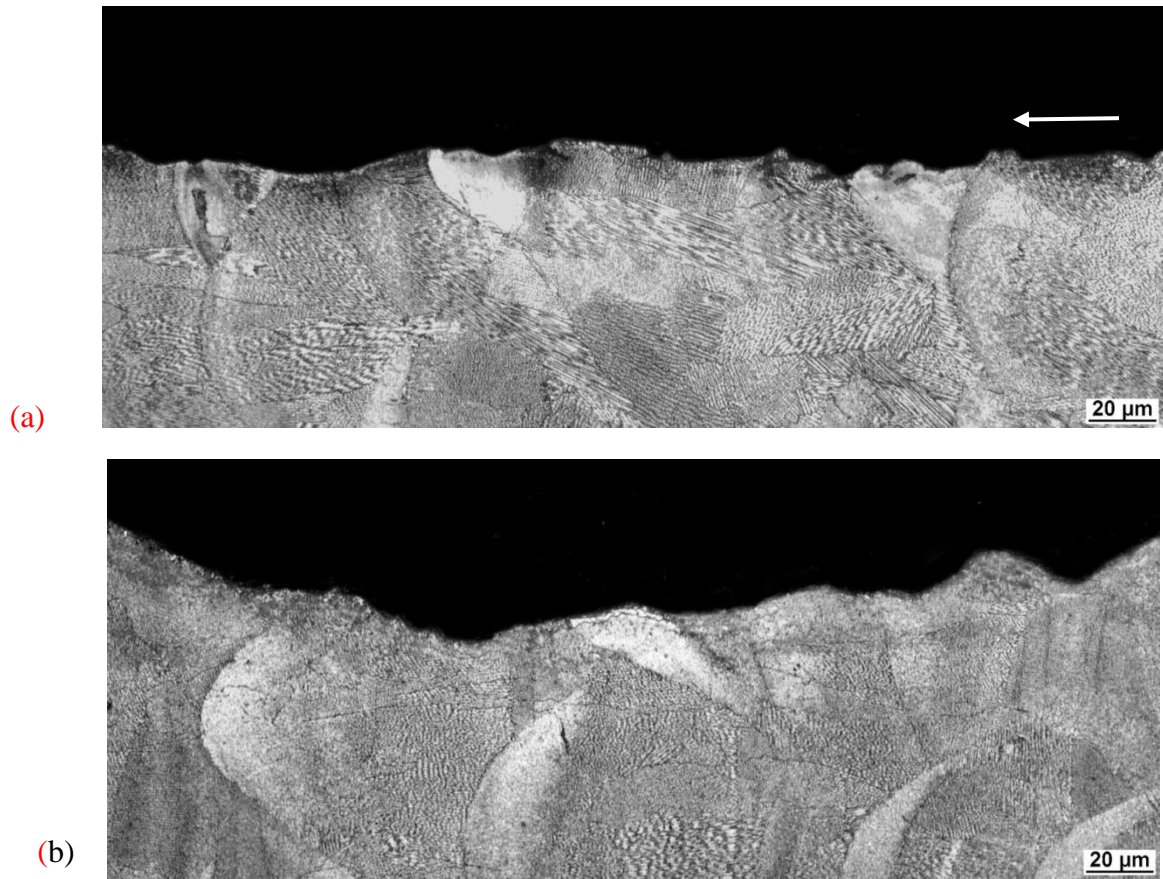


Fig. 11 Fracture profile of crack propagation: (a) $\Delta K = 3.2 \text{ MPam}^{1/2}$, $da/dN \sim 10^{-7} \text{ mm/cycle}$,
(b) $= 10.0 \text{ MPam}^{1/2}$, $da/dN \sim 10^{-5} \text{ mm/cycle}$

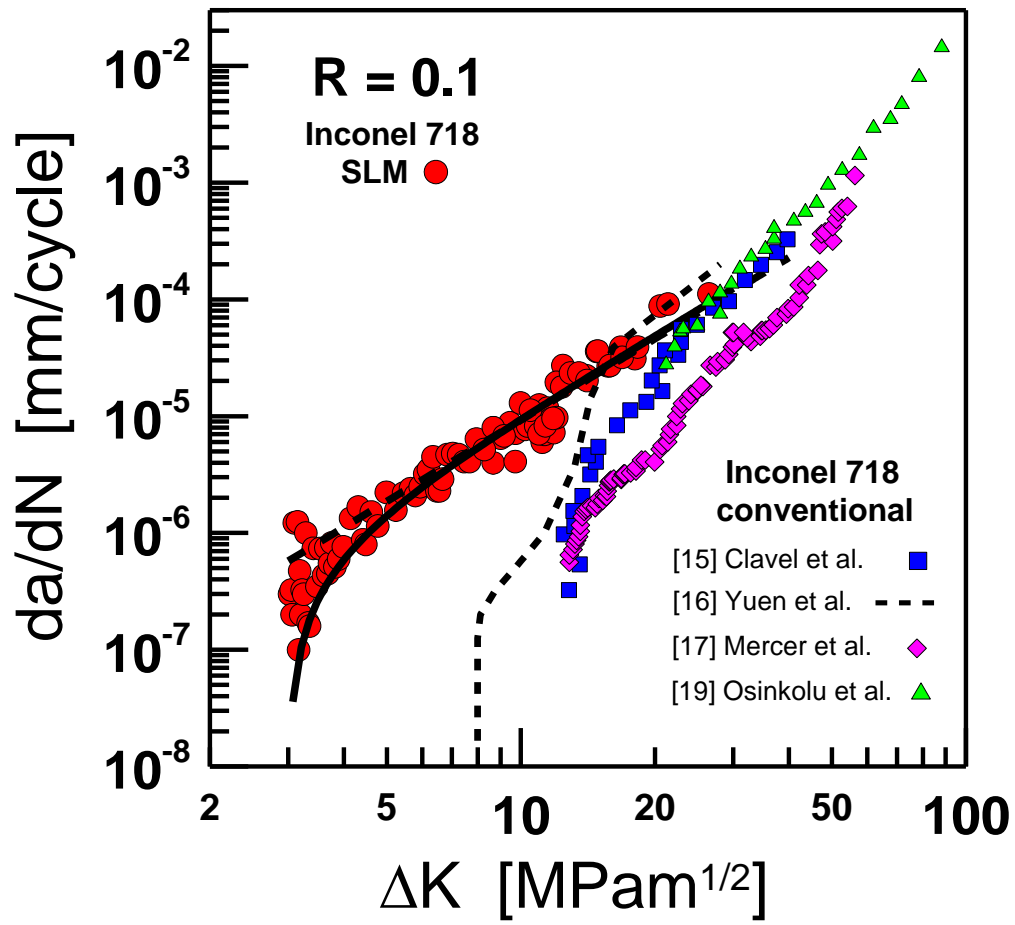


Fig. 12 Comparison of fatigue crack growth data for conventionally and SLM manufactured IN 718